

Analysis of unsteady tip leakage flow in an axial compressor rotor using dynamic mode decomposition

Original article

Article history:

Submission date: 29 November 2023

Acceptance date: 13 July 2024

Publication date: 24 October 2024

This is the updated version of a paper originally presented at the Global Power and Propulsion Technical Conference, GPPS Hong Kong23, October 17–19, 2023.



*Correspondence:

YL: liuyangwei@126.com

Peer review:

Single blind

Copyright:

© 2024 Wei et al. © This is an open access article distributed under the Creative Commons Attribution Non Commercial No Derivatives License (CC BY-NC-ND 4.0). Unrestricted use, distribution, and reproduction of the original work are permitted for noncommercial purposes only, provided it is properly cited and its authors credited. No derivative of this work may be distributed.

Keywords:

axial compressor; DDES; dynamic mode decomposition; tip leakage flow

Citation:

Wei X., Tang Y., Hou J., and Liu Y. (2024). Analysis of unsteady tip leakage flow in an axial compressor rotor using dynamic mode decomposition. *Journal of the Global Power and Propulsion Society*, 8: 405–420.
<https://doi.org/10.33737/jgpps/191168>

Xindi Wei¹, Yumeng Tang¹, Jiexuan Hou¹, Yangwei Liu^{1,*}

¹Beihang University, No. 37, Xueyuan Road, Haidian District, Beijing, China

Abstract

Tip leakage flow (TLF) is an important flow structure in the compressor, and it has a significant effect on the efficiency and stability of the compressor. In this study, dynamic mode decomposition (DMD) is used to study the spatiotemporal flow structure of the tip leakage flow in a compressor rotor. The high-fidelity flow field calculated via the delayed-detached eddy simulation (DDES) of an axial compressor rotor is used as the input dataset for the DMD algorithm. The results show that the unsteady motion of the tip leakage vortex (TLV) is quite different at its generation, development, and dissipation phases. Additionally, three typical unsteady structures, the oscillation of the primary TLV, the TLV breakdown, and the unsteadiness of the unsteady blockage cell, is identified by the DMD modes. Unsteady motions also largely affect the vortex structure and loss generation, especially after the vortex breakdown. The spatiotemporal structure identified by DMD provides a new understanding, which could be helpful for the modeling or flow control of the TLF.

Introduction

Flow in the axial compressor is quite complex because it contains kinds of unsteady flow structures such as the tip leak flow (Booth et al., 1982), the rotor-stator interacting (Liu et al., 2019a, 2023), the corner separation flow (Zhong et al., 2024) and boundary layer transition (Liu et al., 2024c). Among them, tip leakage flow (TLF) is a typical compressor secondary flow caused by the pressure difference between the blade's pressure side and the suction side. The leakage jet interacts with the passage flow and forms the tip leakage vortex (TLV). TLF has a significant effect on the efficiency (Inoue et al., 1986), flow stability (Adamczyk et al., 1993; Tan et al., 2010), and noise generation of the compressor (Hsiao and Chahine, 2005). With the development of the compressor design toward more compact and higher loading, the effect of the TLF is increasingly significant.

Computational fluid dynamics (CFD) has become an important tool for studying compressor flow. In the current design process, the Reynolds-averaged Navier-Stokes (RANS) method is widely used because it is cheap in consumption, and many endeavors have been made to modify turbulence models (Li and Liu, 2022; Liu et al., 2011, 2020, 2023, Liu et al., 2024c). Alternatively, high-fidelity CFD methods, including direct numerical simulations (DNS) and large eddy simulation (LES), can supply detailed information on flow structures, which is critical for flow physics studies and flow control (Xie et al., 2023). Recently, hybrid methods, which combine the

advantages of the Reynolds-averaged Navier-Stokes (RANS) and LES, have drawn increased attention. Hybrid methods use the RANS model to solve the flow within the boundary and use the LES at the main flow. Therefore, it can reach a high accuracy using a much lower computational consumption. Commonly used hybrid methods include DES (Spalart et al., 1997), DDES (Spalart et al., 2006), and GAS (Wang and Liu, 2022). DDES has already been used to study the unsteady flow characteristics of the tip leakage flow in a compressor rotor, and the results are compared with URANS results (Liu et al., 2019b). Then, a physical flow model aimed at simulating the TLF is proposed to reproduce the flow shear mechanism between jet flow and the main flow of tip leakage vortex roll-up (Gao and Liu, 2019). Flow visualization technology, including the pathline and streakline, has also been used to analyze the vortex transportation of the tip leakage vortex under different working conditions based on the results from DDES (Hou et al., 2022). The vortex structures and vortex instability are found to be crucial to describing the TLF, and the advanced vortex identification methods are important tools for studies of TLV, such as the local trace criterion (LT_{cri}) (Liu and Tang, 2019; Liu et al., 2021) and the VR helicity (Tang and Liu, 2022). With the help of the vortex identification method, the different swirling patterns of complex vortices could be distinguished through regional indication. The computational consumption of the high-fidelity method is very large. The RANS method is still widely used in the compressor design stage. Therefore, turbulence modeling for the TLF in RANS simulation is also an important research area (Liu et al., 2008). Traditional turbulence models are found hard to accurately modeling the turbulence characteristic in the TLV (Gao et al., 2016) in a low-speed large-scale axial compressor rotor. Then, a modification of the zonal function is proposed to correct the excessive dissipation of the modeled turbulence kinetic energy (TKE) (Gao and Liu, 2020) in the tip leakage vortex region.

The TLF has been found to be highly unsteady in many previous studies (Zhang et al., 2006; Tong et al., 2007), and its unsteady characteristics affect the noise, blade vibration, and loss generation (Wisler, 1985). Many types of unsteadiness have been reported for TLF. The dynamic interaction of the incoming main flow and the tip leakage flow could induce self-induced unsteadiness in the TLF (Du et al., 2010), and the oscillation of the TLV could also be attributed to an induced vortex and the shock-vortex interaction (Hah et al., 2006). Vortex breakdown is another unsteady flow feature. The breakdown of the TLV could enlarge the blockage region in the tip region (Wang et al., 2021). The stability of the compressor rotor is also related to the unsteadiness of the TLV (Furukawa et al., 1999). Rotating instability vortex are found to be the leading cause of unsteadiness during the development of rotating instability in a low-speed axial flow compressor (März et al., 2002). Therefore, detailed studies on the unsteadiness of TLF are needed to develop new modeling and flow control techniques.

However, extracting key flow features from unsteady flow fields is also challenging because the dataset is massive for high-fidelity simulation results or experimental results. With the progress of computer technology, data-driven approaches have become increasingly prevalent in fluid mechanics, including deep learning, reinforcement learning, modal analysis, etc. These techniques are crucial in feature identification, flow field prediction, and flow control (Liu et al., 2024a,b). Recently, dynamic mode decomposition (DMD) (Schmid, 2010) has been proposed as a data-driven approach to analyze unsteady flow. DMD belongs to the mode analysis method derived from Koopman's theory (Rowley et al., 2009). DMD can extract coherent spatiotemporal structures from time series data. Then, a low-dimensional linear model describing the evolution of these dominant coherent structures can be built. Compared with proper orthogonal decomposition (POD), DMD can provide spatial information in each mode and temporal information embedded in each eigenvalue. This advantage leads to the extensive usage of DMD in analyzing flow phenomena and modeling flow dynamics (Taira et al., 2017; Kunihiko et al., 2020). Application of the DMD or other mode analysis methods has already been conducted in turbomachinery flow, such as the analysis of the pressure pulsation in centrifugal compressor dynamic structures (Zhang et al., 2022) and the analysis of the experimental data to describe the transition process of separation flow (Lengani et al., 2016). Additionally, DMD is also helpful in the development of the reduced order model (ROM) and has been used in isolated airfoils and turbomachinery cascades (Florea and Hall, 1998; Dowell et al., 1999). Since the TLF has abundant unsteady motions, DMD is also valuable for analyzing its flow feature.

This work investigates the unsteady characteristics of the TLF in a rotor based on the unsteady flow field dataset simulated via the DDES. The LT_{cri} method and VR helicity are used to identify the vortex structure, and then DMD for single variables matrix is conducted to extract the spatial-temporal unsteady flow structures. Finally, DMD is conducted for the velocity vector matrix, and the contribution of different DMD modes to the vortex structure of TLV and loss generation are analyzed based on the flow field rebuilt using different modes of the velocity vector.

Case description and numerical method

Test case description

The axial rotor studied in this work is a low-speed compressor that has been tested using the stereoscopic particle image velocimetry (SPIV) method in a low-speed large-scale axial compressor test facility at Beihang University (Liu et al., 2006). The schematic of this experimental rig and the SPIV measurement locations are shown in Figure 1, and the details of the design parameters are summarized in Table 1. The flow in this test compressor, such as the mechanism of the formation and development of the TLV, has also been discussed in our previous papers (Hou and Liu, 2023; Hou et al., 2022). The design point of this rotor is defined as the mass flow coefficient of 0.58, and the near-stall point is defined as the mass flow coefficient of 0.39. The numerical result is validated in our previous work, and the DDES results show a good accordance with the experimental data (Liu et al., 2006).

Numerical method

The software Numeca Autogrid 5 is used to generate a high-quality structure grid. The grid of the rotor blade uses the O4H-type topology. To better capture the structure of TLF in the tip region, the grid within 20% of

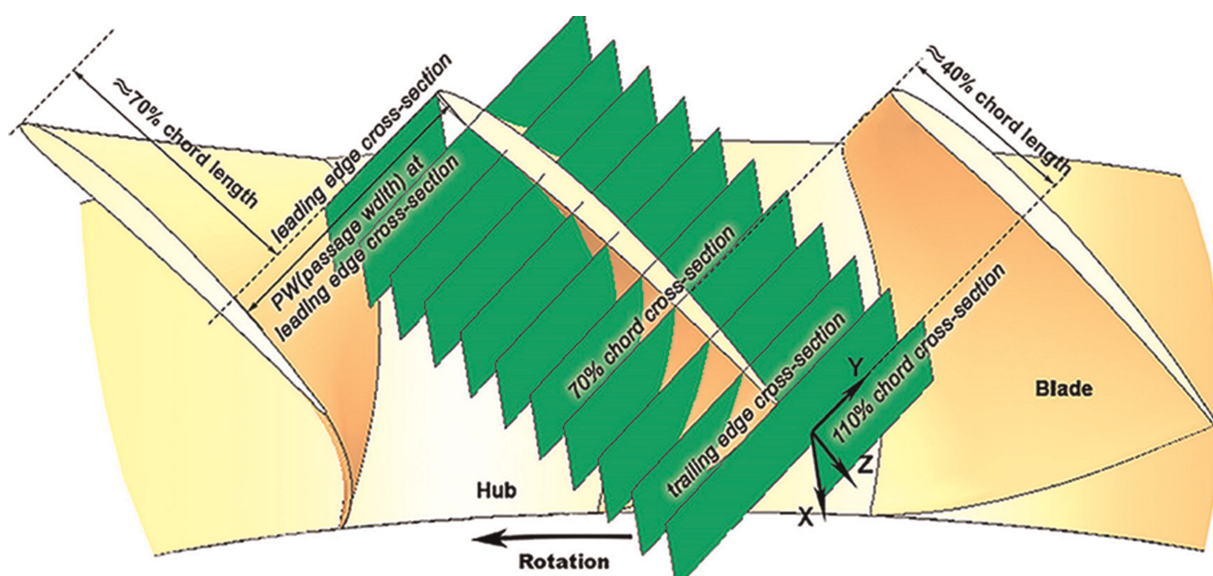


Figure 1. Schematic Layout of the SPIV Measurement Cross Sections of the Axial Rotor (Liu et al., 2008).

Table 1. Parameters of the rotor.

Outer diameter (m)	1.0
Aspect ratio (–)	0.6
Design speed (rpm)	1,200
Flow coefficient in design condition (–)	0.58
Loading coefficient in design condition (–)	0.45
Design mass flow rate (kg/s)	22.4
Reynold number based on the rotor tip chord (–)	7.5×10^5
Inlet guide vane rotor axial gap (mm)	41.9

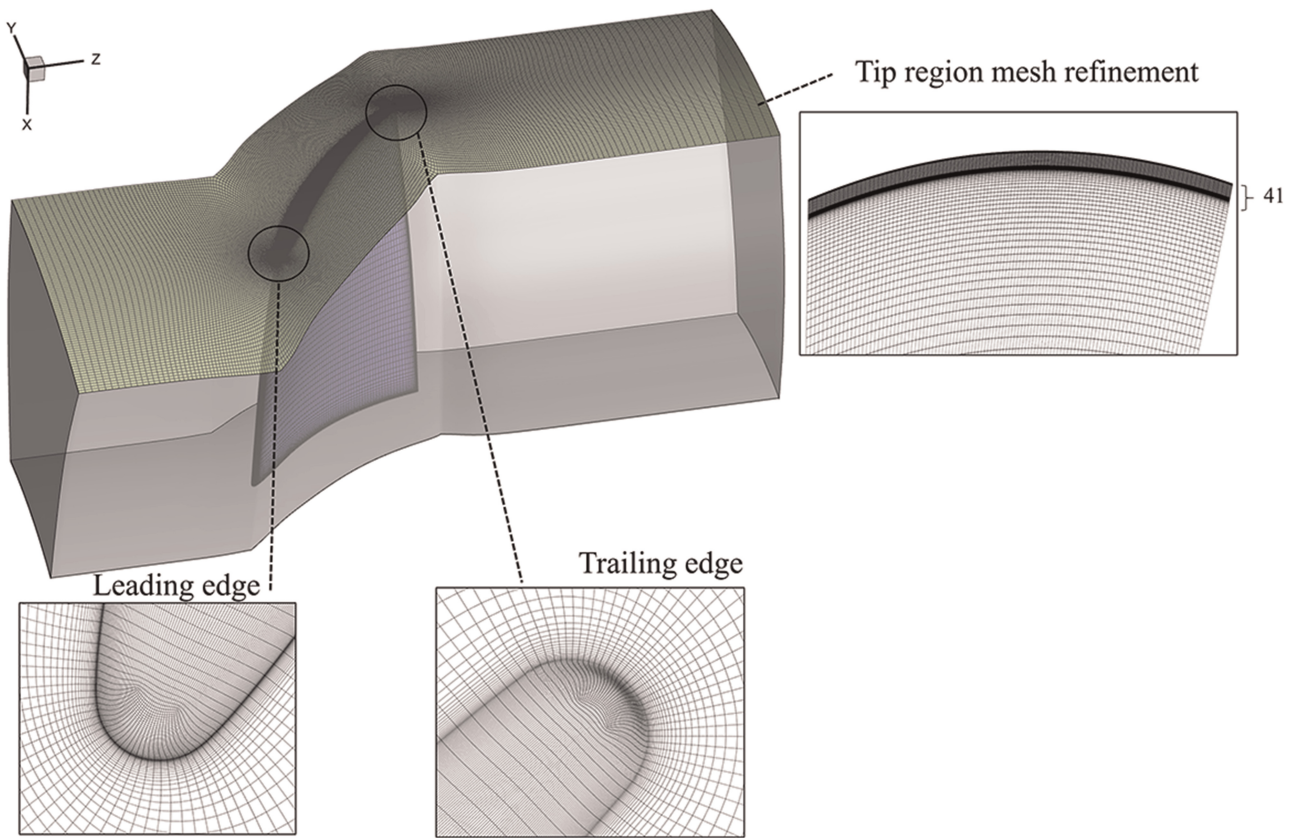


Figure 2. Grid of the Rotor.

the span height to the shroud is refined with a maximum expansion ratio of 1.05. and the grid spacings are kept as $\Delta x + <120$, $\Delta y + <110$, and $\Delta z + <1$, respectively. The total number of grid points is 6.17×10^6 , and details of the final grid are shown in Figure 2.

The numerical simulations use the pressure-based implicit solver from the commercial solver Ansys Fluent and the iterative time advancement solution method is used. The SIMPLE algorithm is used for the simulation. A central differencing scheme is employed for spatial integration, and the implicit second-order time integration is adopted for temporal discretization. The time step for the outer time marching is set to 3×10^{-6} s, which is approximately 1/1,000 times the blade passing the time (TBP), and 30 iterations are set at each inner iteration. The first sample time of the DDES is considered to be $t_{NS}/T_{BP} = 0$ at the near-stall condition. A statistical steady state is reached for all calculations. The instantaneous flow fields are sampled with a time interval (t) of 3×10^{-5} s. More details of the computational setting can be found in our previous work (Liu et al., 2019b).

Dynamic model decomposition

DMD was developed based on the theory of the Koopman operator (Rowley et al., 2009; Schmid, 2010). It is a popular method to extract the temporal-spatial coherent structure in unsteady flow and develop reduced-order modeling (Dowell et al., 1999). Compared with the traditional POD method, DMD could supply more information in the temporal domain. The algorithm of the DMD is introduced as follows. First, snapshots of data must be collected, and these data are arranged as columns of matrices X and Y as follows:

$$\begin{aligned}
 X &= [x(t_1)x(t_2) \cdots x(t_m)] \in \mathbb{R}^{n \times m} \\
 Y &= [x(t_2)x(t_3) \cdots x(t_{m+1})] \in \mathbb{R}^{n \times m}
 \end{aligned}
 \tag{1}$$

Then, the relationship between the snapshots can be considered linearly, as follows

$$X = AY
 \tag{2}$$

The eigenvalues and modes of DMD are defined as the eigenvectors of A . The reduced SVD of X is performed, letting X be denoted as:

$$X = U\Sigma V^T \tag{3}$$

Then let

$$\tilde{A} = U^T A U = U^T Y V \Sigma^{-1} \in \mathbb{R}^{r \times r} \tag{4}$$

Solve the eigenvalues λ_i and eigenvectors $\tilde{\mathbf{v}}_i$ of with $\tilde{A}\tilde{\mathbf{v}}_j = \mu_j\tilde{\mathbf{v}}_j$. The λ_i is the eigenvalue of DMD. Then, the DMD mode \mathbf{v}_i is given by the following:

$$\mathbf{v}_i = \lambda_i^{-1} Y V \sum^{-1} \tilde{\mathbf{v}}_i \tag{5}$$

If we need to rebuild the flow, the initial variant b needs to be calculated through the following equation:

$$b = x(t_1) \cdot \mathbf{v}^{-1} \tag{6}$$

where $x(t_1)$ is the unsteady flow field at the first snapshot. The DMD mode and time eigenvalues are used to rebuild the unsteady flow field as follows:

$$U_{x,k} = \sum_{i=1}^m b_i \cdot \lambda_i^k \cdot \mathbf{v}_i \tag{7}$$

where λ_i is the eigenvalue of matrix A , and the matrix λ_i^k can be written in Vandermonde matrix form as follows:

$$\lambda_i^k = \begin{bmatrix} 1 & \lambda_1^1 & \dots & \lambda_1^{k-1} \\ 1 & \lambda_2^1 & \dots & \lambda_2^{k-1} \\ \vdots & \vdots & \ddots & \vdots \\ 1 & \lambda_m^1 & \dots & \lambda_m^{k-1} \end{bmatrix} \tag{8}$$

Vortex identification method

To study the vortex structures of the TLF, the VR Helicity (Tang and Liu, 2022) and LT_{cri} (Liu and Tang, 2019) methods are utilized. The VR helicity can extract the vortex with a nonzero vorticity component in its rotational axis. The rotational axis of the local vortex is considered to be aligned with the VR direction. The VR helicity density is a strong candidate and Galilean invariance can be guaranteed.

$$\nabla \mathbf{u} = V A V^{-1}$$

$$\nabla \mathbf{u} = [v_r, v_{cr}, v_{ci}] \begin{bmatrix} \lambda_r & 0 & 0 \\ 0 & \lambda_{cr} & \lambda_{ci} \\ 0 & -\lambda_{ci} & \lambda_{cr} \end{bmatrix} [v_r, v_{cr}, v_{ci}]^{-1} \tag{9}$$

$$H_{vR} = \begin{cases} \omega \cdot v_r & \lambda_r \neq 0 \\ 0 & \lambda_r = 0 \end{cases} \tag{10}$$

The local trace criterion (LT_{cri}) with the LT_{cri} -based elliptical region (LTER) is another method to identify the vortex. The magnitude of LT_{cri} is defined as the value of the first invariant of the tensor. The LT_{cri} is

expressed as follows:

$$LT_{\text{cri}} = -\frac{1}{2}\lambda_r^2 - \lambda_{cr}^2 + \lambda_{ci}^2 \quad (11)$$

Furthermore, a projection plane with a divided elliptical region is constructed with LT_{cri} . The projection plane of LT_{cri} (the LT-plane) is also designated as a positive-delta space. The abscissa axis of the LT-plane are defined as $\xi = \lambda_r/|\lambda_{ci}|$, and the ordinate axis is defined as $\eta = \lambda_{cr}/|\lambda_{ci}|$. Figure 3 shows the elliptical region that is defined by $LT_{\text{cri}} > 0$ in the LT plane. The elliptical region is divided into six parts, each region represent a different combination of compressibility and swirling pattern. Parts 1, 2, and 3 represent the expansion pattern, and Parts 4, 5, and 6 represent the compression pattern.

Flow structure of tip leakage flow

3D vortical flow structures identified by the LT_{cri} and the VR helicity are displayed in Figure 4a and b. The primary tip leakage vortex structures are effectively identified via the two methods. In the graphic of LT_{cri} shown in Figure 4a, the threshold is set with an absolute value of $5 \times 10^{-6} \text{ s}^{-2}$. The primary tip leakage vortex is first generated due to the jet from the tip leakage, and then the secondary tip leakage vortex forms in the developing stage of the primary tip leakage vortex. After, the vortex breaks down into small-scale vortices and mixes with the main flow.

In the graphic of the VR helicity method shown in Figure 4b, the threshold has an absolute value of $5,000 \text{ s}^{-1}$. The isosurface colored in blue represents the negative values, and the isosurface colored in red represents the positive values for the helicity methods. The primary tip leakage vortex corresponds to negative values, and the second vortex corresponds to positive values due to the relative movement of the casing. Strong shear in the blade tip region induces a different rotation direction between the primary and second vortex. Furthermore, the normalized helicity methods can extract both strong and weak vortices.

To further study the unsteady motion of the TLF. A streakline and four pathlines, which are selected to represent typical flow particles in the TLF, are drawn in Figure 5a and b, respectively. The streakline and pathline are extracted by recording the path of fluid particles being released at a series of instantaneous times for a specific period (David and Robert, 1995; Hou et al., 2022). Based on the streakline, the primary TLV behaves as an oscillation in a limited range as it is just generated. Downstream, a helical roll-up occurs, and then the TLV suddenly breaks down. At the same time, flow particles disperse in a much larger region than the primary vortex. Figure 5b displays four pathlines passing through the tip leakage vortex, and the axial velocity colors the pathline.

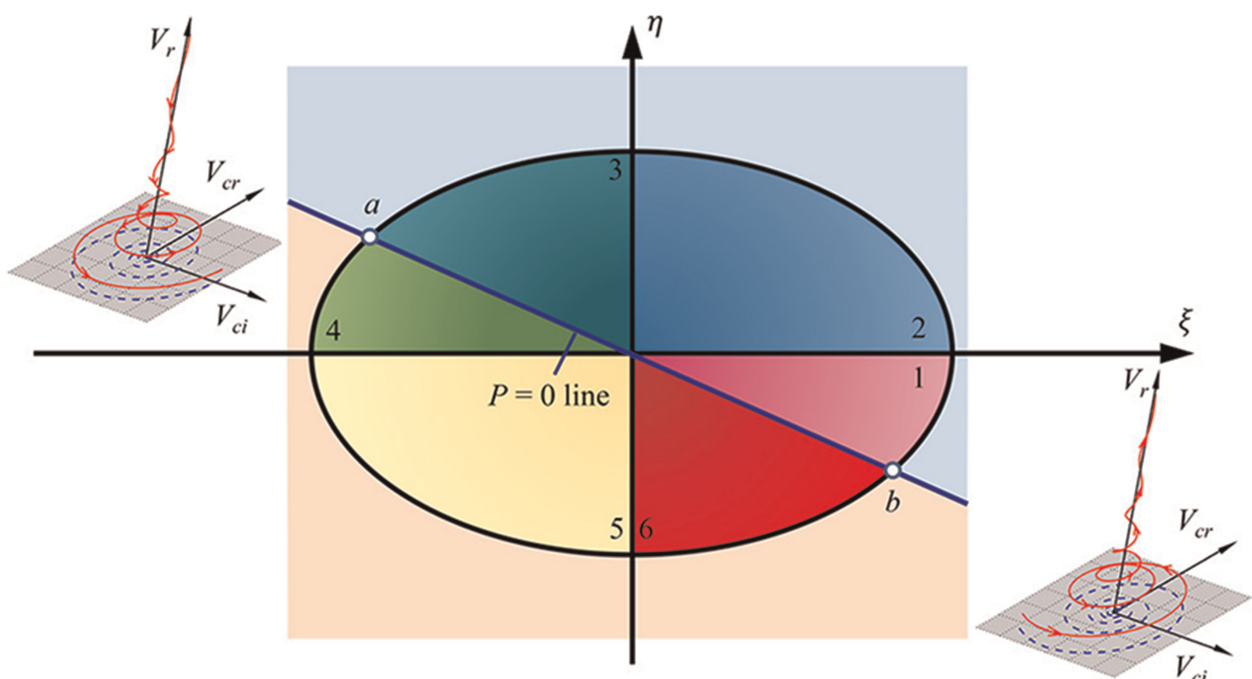


Figure 3. Elliptical Region Characterized by LT_{cri} in LT-plane (Liu and Tang, 2019).

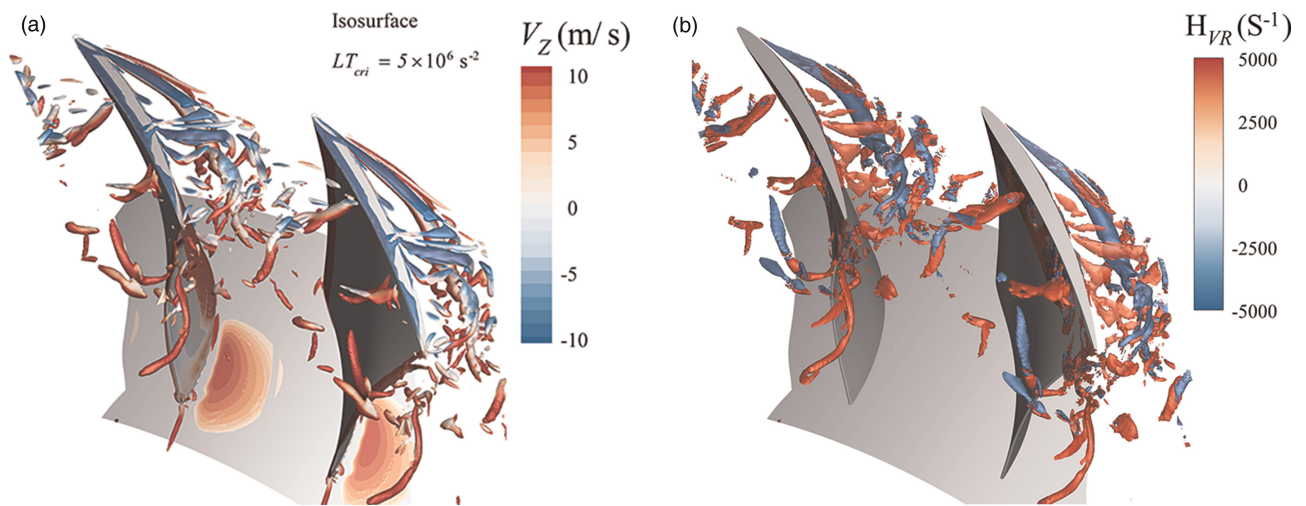


Figure 4. Vortex Structure Under an Instantaneous Flow Field at the Near-Stall Condition. (a) Isosurface of $LT_{cri} = 5 \times 10^6 \text{ (s}^{-2}\text{)}$ and (b) Isosurface of VR helicity = $\pm 5,000 \text{ (s}^{-1}\text{)}$.

Pathline-1 and pathline-2 represent the particles that pass through the primitive TLV and are kept in the original passage. Pathline-3 and pathline-4 represent the particles passing through the primitive TLV and then enter the adjacent passage. Here, pathline-2 is selected for further analysis in Section 4 because it represents the motion of most particles within the TLF at the tip region.

Based on the analysis of the vortex structure and the streamlines, the evolution of the TLV can be divided into three phases (Hou et al., 2022) as shown in Figure 5b. The first phase is the formation or generation phase of the primary TLV, and the second phase is the development of TLV. The breakdown of the primary vortex occurs at the end of the development phase. The third phase is the dissipation process, where the TLF is mixed with the primary passage flow. From the above analysis, the vortex identification method and the streamline can provide much information on a predetermined instantaneous period. However, they cannot extract the spatial-temporal coherent structure for an extended period. As a comparison, the DMD algorithm can deal with the gathered flow field both in space and time, which is crucial to describe the detailed unsteady motion of the TLF.

DMD analysis

This section analyses the 3-dimensional unsteady flow field of this rotor based on the DMD for two single variables at the near stall condition. The time-space matrix for the variable of static pressure P , and the time-space matrix of the radial velocity W_r are conducted DMD separately, and then the mode characteristic and mode shapes are listed and compared.

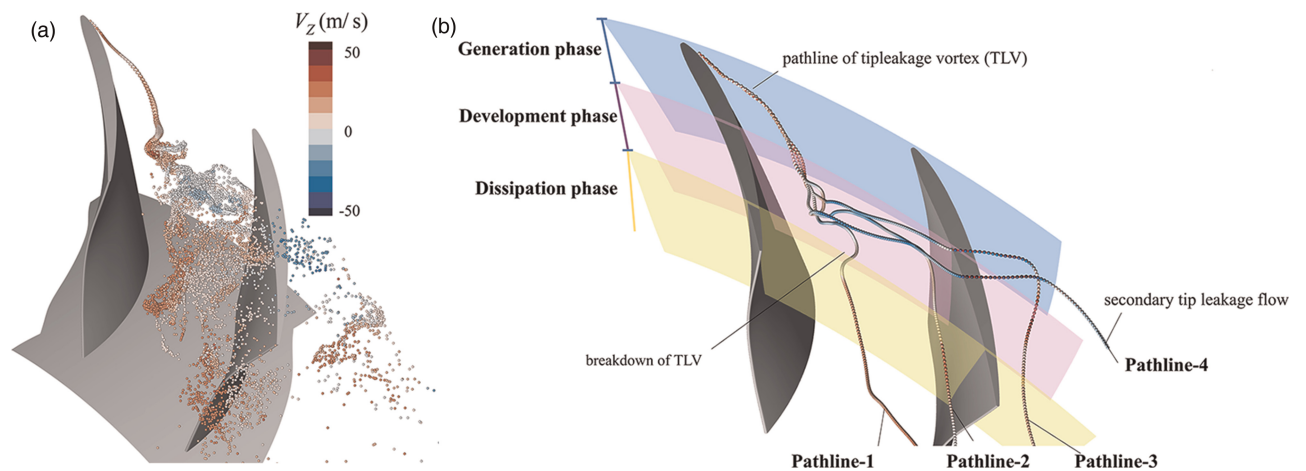


Figure 5. Streakline and Pathlines of the TLF Under the Near Stall Condition. (a) Streaklines (released at the TLV core) and (b) Four typical pathlines of TLV.

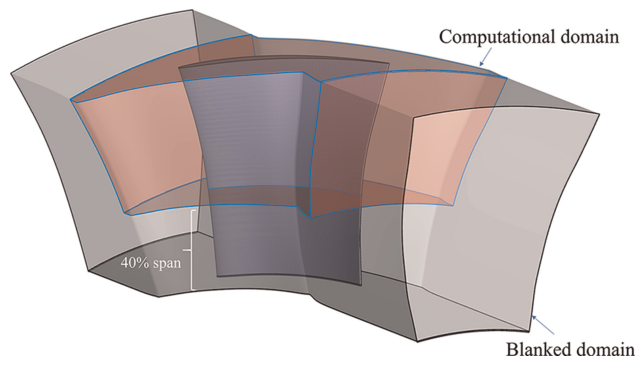


Figure 6. Computational Domain of the DMD.

Overview of DMD characteristics of the TLF

A partial computational domain that contains the tip region is used to reduce the memory requirements, and the location is shown in Figure 6. The total grid number of the computational domain is 3.81 million. In the calculation of DMD, 1,500 snapshots are used, the time interval between two snapshots is 3×10^{-5} s, and the whole time is approximately $15.3 T_{BP}$ ($T_{BP} = 2.94 \times 10^{-4}$ s).

DMD modes in this work are sorted in positive order based on their frequency. This means that the mode with the lowest frequency is marked as mode 1 (the stationary mode), and mode 1 corresponds to the time-averaged flow field in this case. The mode appears in conjugate mode pairs, which share the same altitude and the opposite real value. Mode energy is also calculated to measure the amplitude of the fluctuation corresponding to this mode, which is defined as the time average of the square of each component, as follows:

$$\overline{M_e} = \sum_{i=1}^n \sum_{j=1}^m u^2(x_i, t_j) / m \tag{12}$$

where n is the total number of discrete grid points m is the total time snapshot of the dataset, in this work, n is 3.81 million and m is 1,500. Details of the dataset parameters of DMD are shown in Table 2.

Figure 7a shows the diagram of the mode frequency and mode energy of static pressure, the abscissa represents the mode frequency (normalized by the blade passing frequency, BPF), and the ordinate represents mode energy. Table 3 lists the details of the mode parameters. The mode with 0.57 BPF has the largest mode energy for static pressure, which accounts for 18.1% in total, and the following are modes with frequencies equal to 0.91 BPF and 3.54 BPF. For the radial velocity W_r , the mode with the highest energy corresponds to a frequency of 2.26 BPF, followed by modes with 1.35 BPF and 0.35 BPF.

Figure 8a–c show the isosurface of three typical modes shape of the static pressure P (the value rebuilt by the selected mode at an instantaneous). Mode 2 is located at the suction of the mid-span near the surface at the tip region. Mode 13 is located around the trajectory of the primary tip leakage vortex and the pressure surface of the adjacent rotor. Mode 27 is located around the blockage cell near the pressure surface. The frequencies of mode 2, mode 13, and mode 27 are 0.1 BPF, 0.57 BPF, and 0.91 BPF, respectively. Based on the mode shape and location, it indicates that mode 2 corresponds to the pressure fluctuation around the suction surface. Mode 13 corresponds to the fluctuation caused by the oscillation of the primary TLV. Mode 27 corresponds to the fluctuation of the TLV and the interaction between TLF and the pressure surface. Figure 9a–c show the isosurfaces of mode 10, mode 26, and mode 43 of the radial velocity W_r . Based on the locations and mode shape, it indicates

Table 2. Dataset parameters of the DMD analysis.

Case	Variable	Grid number	Total snapshots	Time interval (T_{INT})	T_S/T_{BP}
1	$P(\text{pa})$	3.81×10^6	1,500	3×10^{-5} s	15.3
2	$w_r(\text{m/s})$	3.81×10^6	1,500	3×10^{-5} s	15.3

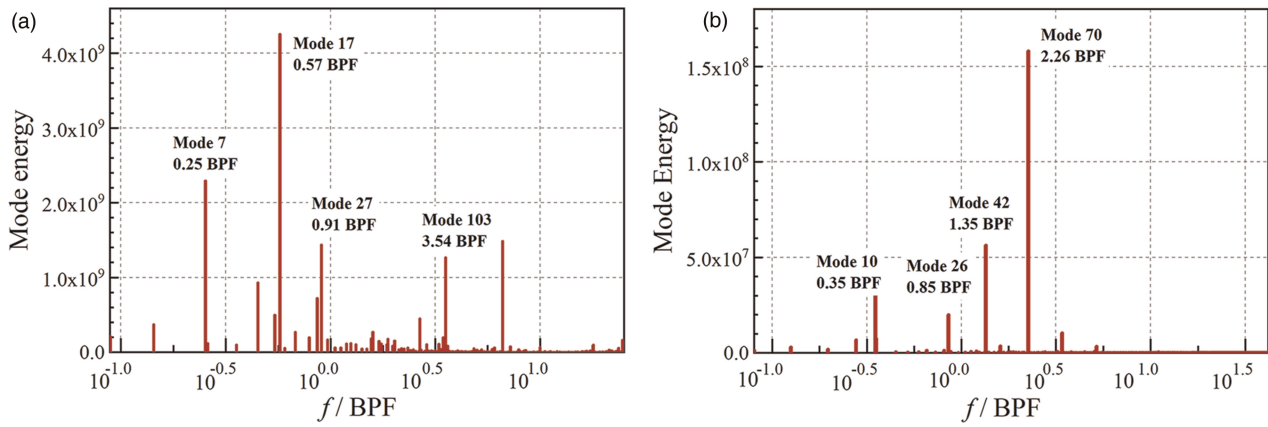


Figure 7. Mode Characteristics of the Static Pressure and Radial Velocity. (a) Frequency-energy diagram of static pressure P and (b) Frequency-energy diagram of the radial velocity W_r .

Table 3. Mode parameters.

	DMD Mode	Frequency (BPF)	Energy proportion
p	13/14	0.25	4.0%
	17/18	0.57	18.1%
	27/28	0.91	6.3%
	103/104	3.54	6.2%
W_r	10/11	0.35	10.3%
	26/27	0.85	7.7%
	42/43	1.35	18.6%
	70/71	2.26	47%

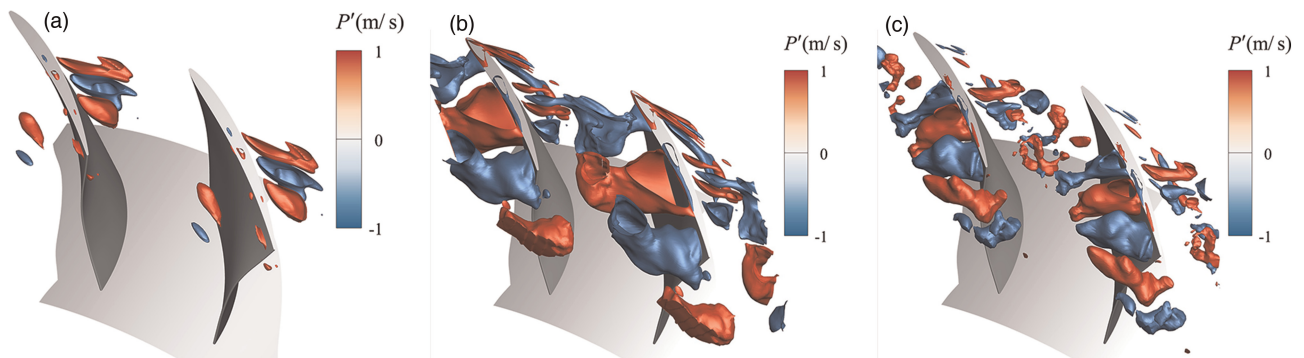


Figure 8. Mode Shape of the Static Pressure P (Pa). (a) Mode 2 (0.1 BPF) isosurface of $P'_2 = \pm 20$, (b) Mode 13 (0.57 BPF) isosurface of $P'_{13} = \pm 300$, and (c) Mode 27 (0.91 BPF) isosurface of $P'_{27} = \pm 100$.

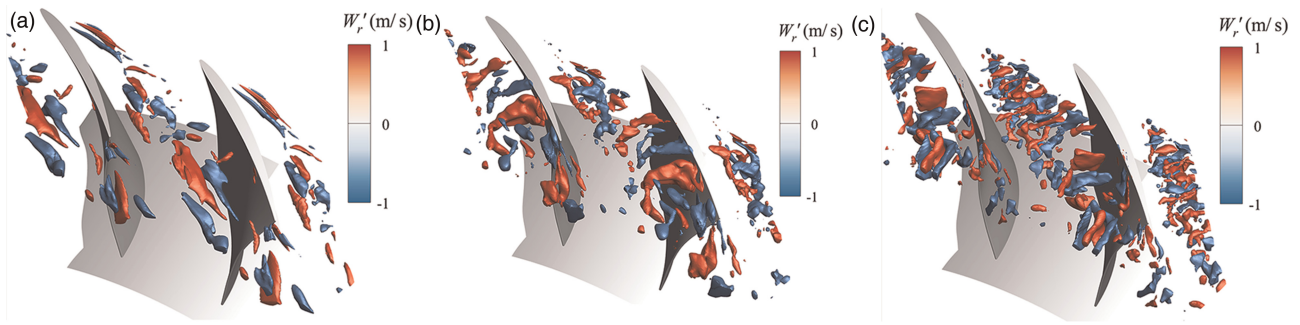


Figure 9. Mode Shape of the Radial Velocity W_r (m/s). (a) Mode 12 (0.35 BPF) isosurface of $W_r'_{12} = \pm 20$, (b) Mode 26 (0.85 BPF) isosurface of $W_r'_{26} = \pm 10$, and (c) Mode 70 (2.26 BPF) isosurface of $W_r'_{70} = \pm 30$.

that mode 12 reflects the motion of the primary TLV, while mode 26 and mode 70 reflect the fluctuation structures at the dissipation phase of the TLF.

Figure 10a–c show the distribution of mode 13 of the static pressure P at 95% span and a meridional surface. At a 95% span, the area with high amplitude is located approximately around the trajectory of the primary TLV. This indicates that the unsteady motion at the generation phase of the TLV oscillates in the tangential direction. Figure 10b and d show the distribution of mode 26 W_r (radial speed in the relative frame of the rotor) at 90% span and a meridional surface. This mode is primarily located near the block cell induced by the TLF, and a negative and positive value appears alternately in the axial direction near the pressure suction surface of the blade. The volume of this mode increases downstream, indicating that the unsteady blockage cell extends its size when transported downstream.

Mode analysis along the pathline

The mode shapes shown above indicate that the TLF is composed of unsteady flow structures with different temporal-spatial scales. The time-space diagram W_r along pathline-2 (shown in Figure 5) is drawn in different phases of the TLF. Figure 11a shows the location of the sampled pathline. Figure 11b and c show the time-space diagram of the original signal and rebuilt signal using the first 100 modes. The abscissa of this diagram is the time, and the coordinate is the non-dimensional axial location. The comparison shows that the signal can be

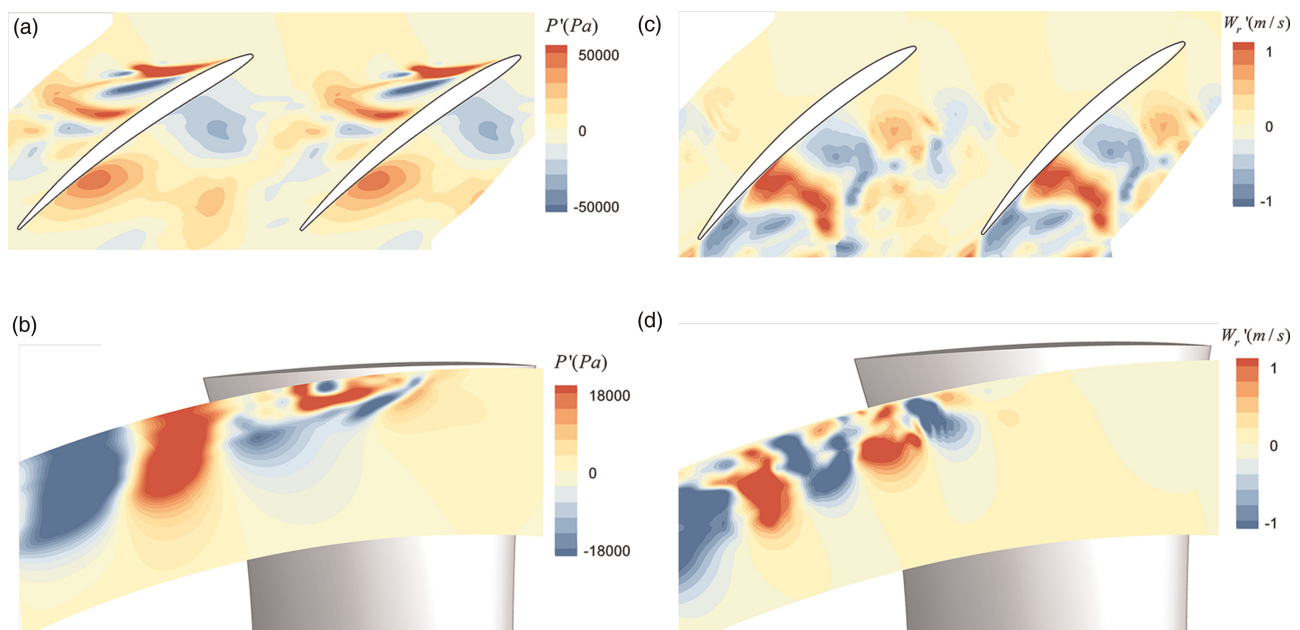


Figure 10. Two-Dimensional Distribution of the DMD Modes. (a) Mode 13 of P (Pa) at 95% span, (b) Mode 26 of W_r (m/s) at 90% span, (c) Mode 13 of P (Pa) at a meridional surface, and (d) Mode 26 of W_r (m/s) at a meridional surface.

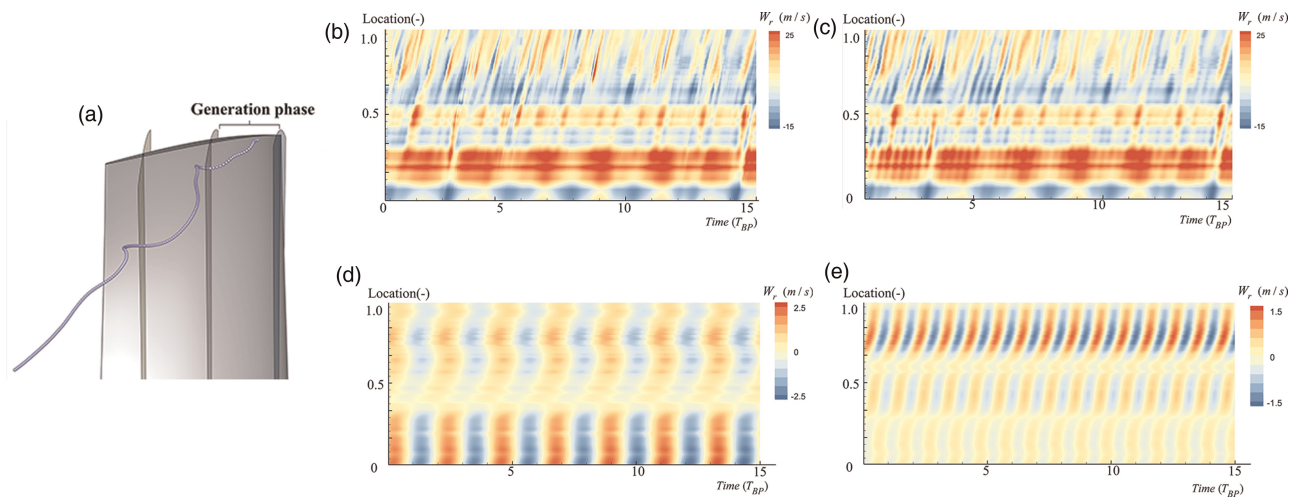


Figure 11. Time-space Diagram of W_r (m/s) along the Vortex Core at the Generation Phase. (a) Sampling line, (b) Original W_r , (c) W_r rebuilt from 1 to 100 modes, (d) W_r rebuilt by Mode 10 (0.35 BPF) and (e) W_r rebuilt by mode 33 (1.04 BPF).

effectively rebuilt using only the first 100 modes at the start of the trajectory. However, as the TLV transports downstream, some high-frequency signals occur. Figure 11d and e display two primary mode signals with frequencies of 0.35 BPF and 0.85 BPF, accounting for most of the total signal. The space-time diagram shown in Figure 11 shows that the oscillating frequency is approximately 0.35 BPF at the start along the vortex core, and then this signal decreases, while the signal with 0.85 BPF suddenly increases.

Then, the time-space diagram of the original and rebuilt signal at the development phase of the line is displayed in Figure 12b and c, and the location of the development phase in the streamline is shown in Figure 12a. At this phase, the primary TLV interacts with other flow structures, such as the vortex rope (Hou et al, 2022), and it finally breaks down into vortices with smaller scales. Figure 12c and d show two primary modes rebuilt by modes 13 and 27. This indicates that the frequency of the primary mode is much higher than that of the generation stage, which is approximately 1.35 BPF and 2.26 BPF, respectively.

Figure 13b and c show the original and rebuilt spatial-temporal signal W_r from the 70% chord at pathline-2, and the location of the dissipation phase is shown in Figure 13a. The periodicity of the signal at this phase is also significant. Figure 13c and d show two of the primary DMD modes with a frequency of 0.45 BPF and 1.49 BPF. It indicates that the signal with the lower frequency component increases amplitude as the particle moves downstream.

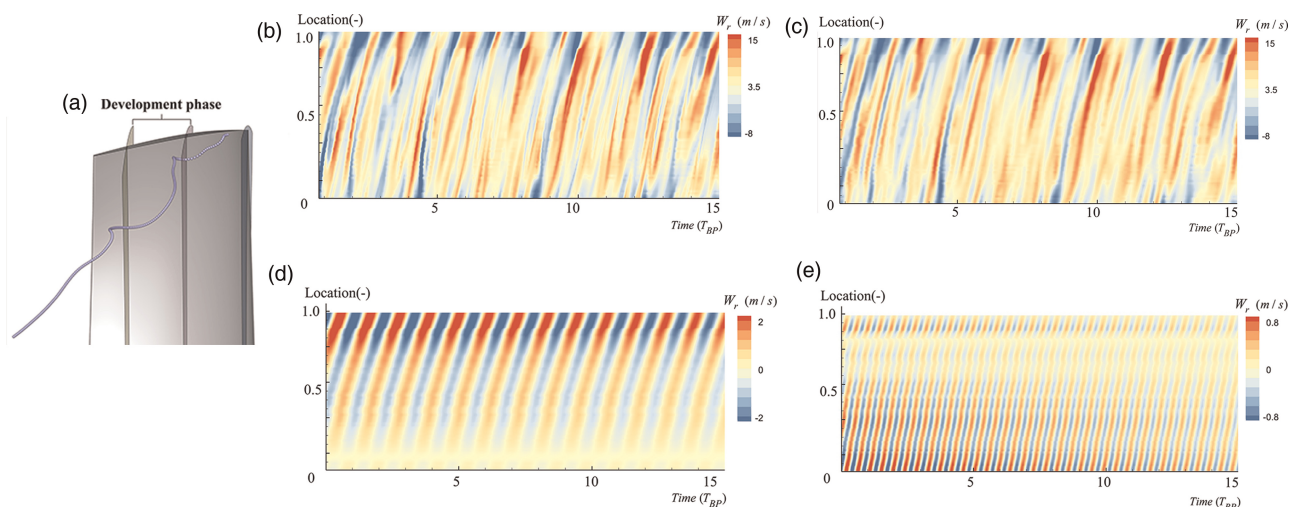


Figure 12. Time-space Diagram of W_r (m/s) along the Vortex Vore at the Development Phase. (a) Sampling line, (b) Original W_r , (c) Rebuilt W_r from 1 to 100 modes, (d) Rebuilt W_r by Mode 42 (1.35 BPF), and (e) W_r rebuilt by mode 70 (2.26 BPF).

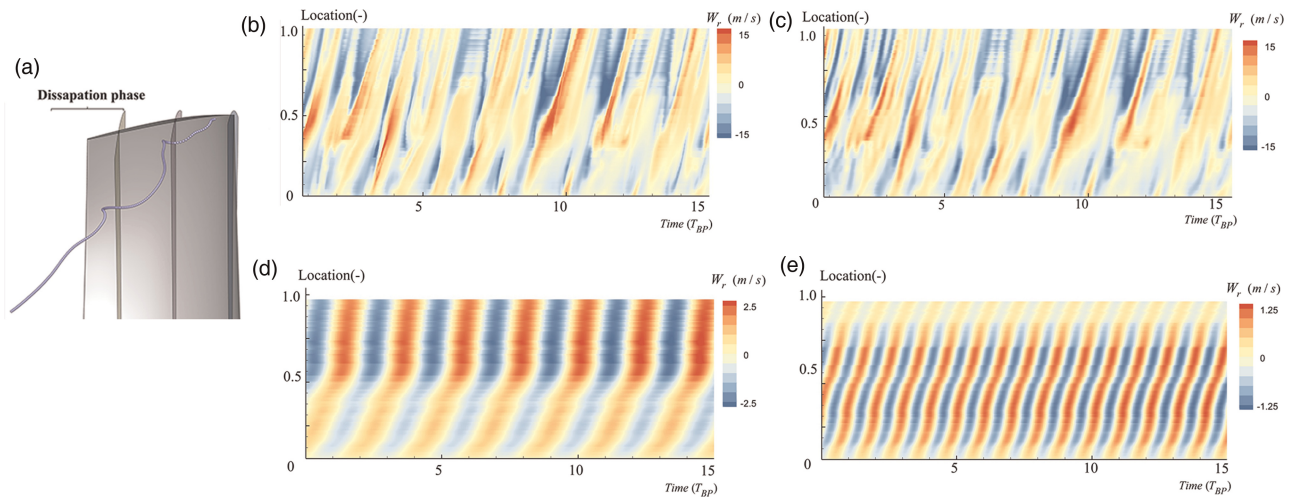


Figure 13. Time-Space Diagram of W_r Along the Vortex Core at the Dissipation Phase. (a) Sampling line, (b) Original W_r , (c) Rebuilt W_r from 1 to 100 modes, (d), Rebuilt W_r by mode 12(0.35 BPF), and (e) Rebuilt W_r by mode 26(0.85 BPF).

The above analysis indicates that the TLV has three typical unsteady characteristics at its generation, development, and dissipation phases. In the generation phase, the primary TLV has an oscillation motion with a frequency of about 0.35 BPF. Then at the development phase, some small-scale flow structures are generated due to the breakdown of the primary TLV, and the periodicity of the fluctuation is weakened. Finally, the periodicity of the fluctuation is rebuilt in the dissipation phase, with a frequency of approximately 0.85 BPF.

Effect of the DMD mode on the vortex structure and loss generation

This section studies the effect of the DMD mode on the formation of vortex structures and loss generation. The flow field is rebuilt using different numbers of the DMD mode, and then the LT_{cri} method is used to identify the vortex structure. In addition, the unsteady loss is also analyzed based on the entropy production rate.

To recover the entire velocity vector flow field, DMD is conducted on the variable matrix X , which is defined as follows:

$$X = \begin{bmatrix} W_{xt_1} & W_{xt_2} & \dots & W_{xt_m} \\ W_{yt_1} & W_{yt_2} & \dots & W_{yt_m} \\ W_{zt_1} & W_{zt_2} & \dots & W_{zt_m} \end{bmatrix} \quad (13)$$

where W_{xt_i} , W_{yt_i} , and W_{zt_i} are the velocity components in three directions of the entire flow field at an instant. Five hundred snapshots are used to build the spatial-temporal matrix X , and the space domain is kept the same as shown in Figure 6. The DMD mode is also ranked ascending by frequency in this section. It should be noted that the mode characteristics are different from those in Section 4 since their input dataset matrix is different.

Effect of modes on the vortex structure

Based on the results shown in Section 4, the motion of vortices with TLF is unsteady, especially at the development and dissipation phases. On the other hand, the unsteady flow field can be rebuilt by different modes corresponding to different spatial-temporal flow structures. Figure 14 shows the isosurface of LT_{cri} with the threshold equal to $8 \times 10^6 \text{s}^{-2}$, and the isosurface is colored by the number of quadrants in LTER. Figure 14a–d shows the vortex structures rebuilt using mode 1, modes from 1 to 3, 1 to 6, and 1 to 100, respectively. The isosurface of LT_{cri} in the original unsteady flow field is also shown in Figure 14e. It should be noticed that the mode 1 is the stationary mode corresponding to the time average flow field with a zero-decay rate. The comparison indicates that the primary TLV at the generation phase is effectively recovered by the stationary mode, while the small-scale unsteady vortex structure, including part of the second tip leakage vortex (S-TLV), is filtered. If mode 3 and mode 5 are used, the S-TLV can be recovered. A comparison between the vortex structure rebuilt using different modes also shows that the interaction between the primary TLV and vortex rope is an unsteady process, it cannot be recovered by the stationary component. In addition, more small-scale vortices appear at the

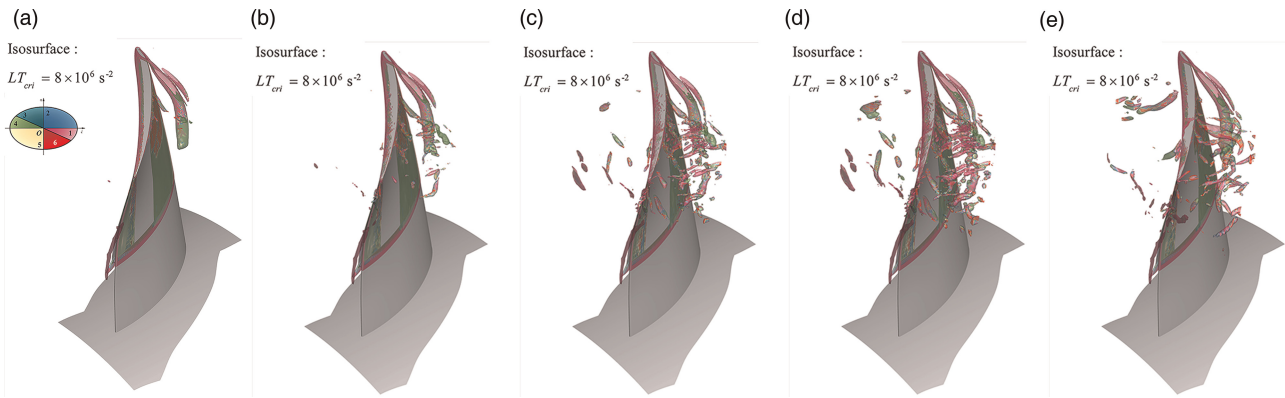


Figure 14. Vortex Structures at an Instantaneous Flow Field. (a) Rebuilt by mode 1, (b) Rebuilt from mode 1 to mode 3, (c) Rebuilt from mode 1 to mode 6, (d) Rebuilt from mode 1 to mode 100, and (e) Original unsteady flow field.

development and dissipation phases. Figure 14e shows that the entire vortex structure can be recovered if all modes were used to rebuild the flow field.

Based on the LTER indication, vortices with different vortical flow patterns can be distinguished. Figure 14a shows the time-averaged TLV is in the expansion state as it just generates, and then the TLV turns into the compression state at approximately 10% chord downstream. As the mode number used to rebuild the flow field increases to three, vortices in the compression state occur at the end of the primary TLV. Those small-scale unsteady vortices recovered by mode 3 to mode 6, primarily located in the vortex interaction and breakdown regions, are in the expansion state.

Effect of modes on the entropy production

Vortex flow can produce irreversible viscosity loss and, therefore, has a large effect on the efficiency of the rotor. The loss induced by viscosity can be quantitated by the viscosity entropy production rate (Moore and Moore, 1983), which is defined as follows:

$$\dot{S}_{\text{visc}} = \frac{2\mu\bar{s}_{ij}\bar{s}'_{ij}}{\bar{T}} + \frac{2\mu s'_{ij} s'_{ij}}{\bar{T}} \tag{14}$$

where μ represents the molecular viscosity coefficient, \bar{s}_{ij} represents the time average strain ratio, s'_{ij} represents the instantaneous fluctuation of the strain ratio, and \bar{T} is the time-averaged temperature (288.15 K used in this case). Equation (13) shows that the viscosity loss is composed of time-averaged and instantaneous components. Therefore, the entropy production is highly correlated to the unsteady vortex structure through the instantaneous item. Figure 15a and b show the \dot{S}_{visc} at an instantaneous and time-averaged flow field. The time-averaged \dot{S}_{visc} is consistent with the total \dot{S}_{visc} at the generation phase of the TLV, indicating that the entropy production is mainly composed of its steady component before the primary TLV breakdown. In addition, the area with a high entropy production rate is located at the edge of the primary TLV. Figure 15c and d display the \dot{S}_{visc} obtained by DMD mode 2 and mode 4. The area with high \dot{S}_{visc} in mode 2 is located at the center region of the TLF at

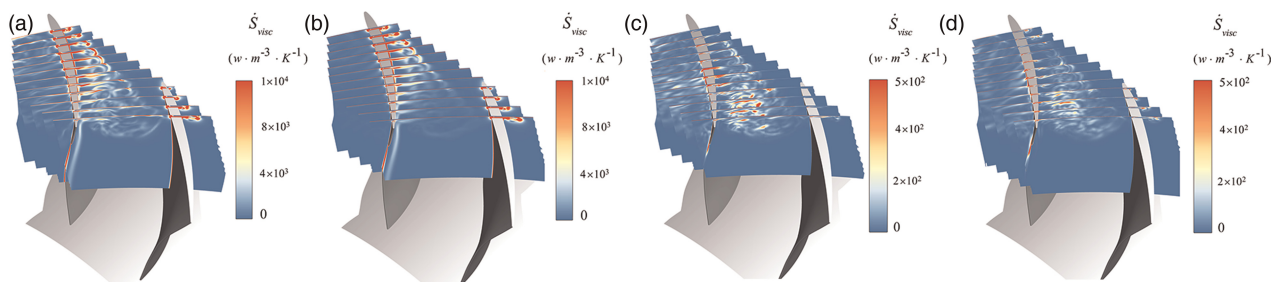


Figure 15. Energy Production at an Instantaneous Flow Field. (a) \dot{S}_{visc} at an instantaneous flow field, (b) Time-averaged \dot{S}_{visc} , (c) \dot{S}_{visc} in the flow field rebuilt by mode 2/3 (d), and \dot{S}_{visc} in the flow field rebuilt by mode 3/4.

the dissipation phase. As a comparison, mode 4 is near the hub of the dissipation phase. The loss produced by mode 4 is also smaller than that produced by mode 2 in amplitude.

Conclusion

This work investigates the unsteady tip leakage flow of a rotor under the near-stall condition. First, DMD is used for the 3D flow field calculated via DDES to extract the spatial-temporal structures. Next, the unsteady characteristics are analyzed based on the different modes. Finally, the effect of flow unsteadiness on the vortex structure and loss generation is analyzed. The conclusions of this work can be drawn as follows.

1. In the generation phase of the TLV, the unsteadiness behaves as the oscillation of the primary TLV. In the development phase of TLV, the unsteadiness of TLV behaves as the interaction between the primary TLV and other vortex structures. In the dissipation phase, TLV finally breaks down into small-scale unsteady vortices.
2. Unsteady motions of the tip leakage vortex can be reflected by the different DMD modes. The unsteady fluctuation of the vortex rope has a relatively lower frequency, and it is reflected by the first 2 modes. The unsteady motion of the main TLV has the highest fluctuation amplitude and corresponds to pressure mode 13. DMD can also provide information about the frequency and amplitude of different unsteady motions.
3. Vortex structures and loss generations can be divided into steady and different unsteady components through DMD. In the generation phase, entropy production is primarily composed of its steady component. Conversely, vortex structure and loss generation are mainly composed of unsteady components after the primary TLV breakdown.

The mode information provided by DMD facilitates a novel view to describe the motion of the TLF. The dynamic characteristics are also valuable for the development of data-driven modeling or flow control methods for the TLF.

Nomenclature

BPF	blade passing frequency
T_{BP}	blade passing time
TLF	tip leakage flow
TLV	tip leakage vortex
W	relative velocity
\dot{S}	entropy production
f	frequency
v_i, v_j, v_k	velocity components for the spatial point
u'	velocity fluctuation
μ	molecular viscosity [kg/(m·s)]
ω	vorticity vector
s_{ij}	strain rate tensor
v_{ci}	eigenvector of $\nabla \mathbf{u}$ according to λ_{ci}
v_{cr}	eigenvector of $\nabla \mathbf{u}$ according to λ_{cr}
v_r	eigenvector of $\nabla \mathbf{u}$ according to λ_r
r	radial direction
z	axial direction
t	tangential direction

Greek symbols

λ_{ci}	the imaginary part of the complex eigenvalue of $\nabla \mathbf{u}$
λ_{cr}	the real part of the complex eigenvalue of $\nabla \mathbf{u}$
λ_r	the real eigenvalue of $\nabla \mathbf{u}$ when $\Delta > 0$
Ω	vorticity tensor
Δ	discriminant of the velocity gradient tensor

Funding sources

This work was supported by the National Natural Science Foundation of China (Nos. 51976006 and 52106039), the Fundamental Research Funds for the Central Universities, the National Science and Technology Major Project (No. 2017-II-003-0015), the Aeronautical Science Foundation of China (No. 2018ZB51013), Science Center for Gas Turbine Project (No. P2022-B-II-005-001), and the Academic Excellence Foundation of BUAA for PhD Students.

Competing interests

Xindi Wei declares that he has no conflict of interest. Yumeng Tang declares that she has no conflict of interest. Jiexuan Hou declares that she has no conflict of interest. Yangwei Liu declares that he has no conflict of interest.

References

- Adamczyk J. J., Celestina M. L., and Greitzer E. M. (1993). The role of tip clearance in high-speed fan stall. *Journal of Turbomachinery*. 115 (1): 28–38. <https://doi.org/10.1115/1.2929212>.
- Booth T. C., Dodge P. R., and Hepworth H. K. (1982). Rotor-tip leakage: part I—basic methodology. *Journal of Engineering for Power*. 104 (1): 154–161. <https://doi.org/10.1115/1.3227244>.
- David S. and Robert H. (1995). Identification of swirling flow in 3-D vector fields. In AIAA Paper No. 1995-1715. <https://doi.org/10.2514/6.1995-1715>.
- Dowell E. H., Hall K. C., Thomas J., Florea R., Epureanu B., and Heeg J. (1999). Reduced order models in unsteady aerodynamics. In AIAA Paper No. 1999-1261. <https://doi.org/10.2514/6.1999-1261>.
- Du J., Lin F., Zhang H., and Chen J. (2010). Numerical investigation on the self-induced unsteadiness in tip leakage flow for a transonic fan rotor. *Journal of Turbomachinery*. 132 (2): 021017. <https://doi.org/10.1115/1.3145103>.
- Furukawa M., Inoue M., Saiki K., and Yamada K. (1999). The role of tip leakage vortex breakdown in compressor rotor aerodynamics. *Journal of Turbomachinery*. 121 (3): 469–480. <https://doi.org/10.1016/10.1115/1.2841339>.
- Florea R. and Hall K. C. (1998). Eigenmode analysis of unsteady flows about airfoils. *Journal of Computational Physics*. 147 (2): 568–593. <https://doi.org/10.1006/jcph.1998.6102>.
- Gao Y. and Liu Y. (2019). A flow model for tip leakage flow in turbomachinery using a square duct with a longitudinal slit. *Aerospace Science and Technology*. 95: 105460. <https://doi.org/10.1016/j.ast.2019.105460>.
- Gao Y. and Liu Y. (2020). Modification of DDES based on SST $k-\omega$ model for tip leakage flow in turbomachinery. In ASME Paper No. GT2020-14851. <https://doi.org/10.1115/gt2020-14851>.
- Gao Y., Liu Y., Zhong L., Hou J., and Lu L. (2016). Study of the standard $k-\varepsilon$ model for tip leakage flow in an axial compressor rotor. *International Journal of Turbo and Jet Engines*. 33 (4): 353–360. <https://doi.org/10.1515/tjj-2015-0039>.
- Hah C., Bergner J., and Schiffer H. (2006). Short length-scale rotating stall inception in a transonic axial compressor—criteria and mechanisms. In ASME Paper No. GT2006-90045. <https://doi.org/10.1115/GT2006-90045>.
- Hou J. and Liu Y. (2023). Evolution of unsteady vortex structures in the tip region of an axial compressor rotor. *Physics of Fluids*. 35 (4): 045107. <https://doi.org/10.1063/5.0141818>.
- Hou J., Liu Y., Zhong L., Zhong W., and Tang Y. (2022). Effect of vorticity transport on flow structure in the tip region of axial compressors. *Physics of Fluids*. 34 (5): 055102. <https://doi.org/10.1063/5.0087833>.
- Hsiao C.-T. and Chahine G. L. (2005). Scaling of tip vortex cavitation inception noise with a bubble dynamics model accounting for nuclei size distribution. *Journal of Fluids Engineering*. 127 (1): 55–65. <https://doi.org/10.1115/1.1852476>.
- Inoue M., Kuroumaru M., and Fukuhara M. (1986). Behavior of tip leakage flow behind an axial compressor rotor. *Journal of Engineering for Gas Turbines and Power*. 108 (1): 7–14. <https://doi.org/10.1115/1.3239889>.
- Kunihiko T., Hemati M., Brunton S., Sun Y., Duraisamy K., et al. (2020). Modal analysis of fluid flows: Applications and outlook. *AIAA Journal*. 58 (3): 998–1022. <https://doi.org/10.2514/1.J058462>.
- Lengani D., Simoni D., Ubaldi M., Zunino P., and Bertini F. (2016). Experimental investigation on the time–space evolution of a laminar separation bubble by proper orthogonal decomposition and dynamic mode decomposition. *Journal of Turbomachinery*. 139 (3): 031006. <https://doi.org/10.1115/1.4034917>.
- Li W. and Liu Y. (2022). Numerical investigation of corner separation flow using Spalart-Allmaras model with various modifications. *Aerospace Science and Technology*. 127: 107682. <https://doi.org/10.1016/j.ast.2022.107682>.
- Li W., and Liu Y. (2023). Study of limits to the rotation function in the SA-RC turbulence model. *Chinese Journal of Aeronautics*. 36 (1): 246–265. <https://doi.org/10.1016/j.cja.2022.05.015>.
- Liu Y., and Tang Y. (2019). An elliptical region method for identifying a vortex with indications of its compressibility and swirling pattern. *Aerospace Science and Technology*. 95: 105448. <https://doi.org/10.1016/j.ast.2019.105448>.
- Liu B., Yu X., Liu H., Jiang H., Yuan H., and Xu Y. (2006). Application of SPIV in turbomachinery. *Experiments in Fluids*. 40: 621–642. <https://doi.org/10.1007/s00348-005-0102-9>.
- Liu Y., Yu X., and Liu B. (2008). Turbulence models assessment for large-scale tip vortices in an axial compressor rotor. *Journal of Propulsion and Power*. 24 (1): 15–25. <https://doi.org/10.2514/1.26134>.
- Liu Y., Lu L., Fang L., and Gao F. (2011). Modification of Spalart-Allmaras model with consideration of turbulence energy backscatter using velocity helicity. *Physics Letters A*. 375 (24): 2377–2381. <https://doi.org/10.1016/j.physleta.2011.05.023>.
- Liu Y., Tang Y., Liu B., and Lu L. (2019a). An exponential decay model for the deterministic correlations in axial compressors. *Journal of Turbomachinery*. 141 (2): 021005. <https://doi.org/10.1115/1.4041380>.
- Liu Y., Zhong L., and Lu L. (2019b). Comparison of DDES and URANS for unsteady tip leakage flow in an axial compressor rotor. *Journal of Fluids Engineering*. 141 (12): 121405. <https://doi.org/10.1115/1.4043774>.

- Liu Y., Tang Y., Tucker P. G., and Scillitoe A. D. (2020). Modification of shear stress transport turbulence model using helicity for predicting corner separation flow in a linear compressor cascade. *Journal of Turbomachinery*. 142 (2): 021004. <https://doi.org/10.1115/1.4045658>.
- Liu Y., Zhong W., and Tang Y. (2021). On the relationships between different vortex identification methods based on local trace criterion. *Physics of Fluids*. 33 (10): 105116. <https://doi.org/10.1063/5.0063326>.
- Liu Y., Wei X., and Tang Y. (2023). Investigation of unsteady rotor–stator interaction and deterministic correlation analysis in a transonic compressor stage. *Journal of Turbomachinery*. 145 (7): 071004. <https://doi.org/10.1115/1.4056716>.
- Liu Y., Zhao S., Wang F., and Tang Y. (2024a). A novel method for predicting fluid–structure interaction with large deformation based on masked deep neural network. *Physics of Fluids*. 36 (2): 027103. <https://doi.org/10.1063/5.0183290>.
- Liu Y., Wang F., Zhao S., and Tang Y. (2024b). A novel framework for predicting active flow control by combining deep reinforcement learning and masked deep neural network. *Physics of Fluids*. 36 (3): 037112. <https://doi.org/10.1063/5.0194264>.
- Liu Y., Luo P., and Tang Y. (2024c). Improved prediction of turbomachinery flows using Reynolds stress model with γ transition model. *Aerospace Science and Technology*. 144: 108812. <https://doi.org/10.1016/j.ast.2023.108812>.
- März J., Hah C., and Neise W. (2002). An Experimental and Numerical Investigation into the Mechanisms of Rotating Instability. *Journal of Turbomachinery*. 124 (3): 367–374. <https://doi.org/10.1016/10.1115/1.1460915>.
- Moore J. and Moore J. (1983). Entropy production rates from viscous flow calculations: Part I - A turbulent boundary layer flow. In ASME Paper No. GT1983-70. <https://doi.org/10.1115/83-gt-70>.
- Rowley C., Mezić I., Bagheri S., Schlatter P., and Henningson D. (2009). Spectral analysis of nonlinear flows. *Journal of Fluid Mechanics*. 641: 115–127. <https://doi.org/10.1017/S0022112009992059>.
- Schmid P. J. (2010). Dynamic mode decomposition of numerical and experimental data. *Journal of Fluid Mechanics*. 656: 5–28. <https://doi.org/10.1017/S0022112010001217>.
- Spalart P. R., Jou W. H., Strelets M., and Allmaras, S. (1997). Comments on the feasibility of LES for wings, and on a hybrid RANS/LES approach. In Proceedings of first AFOSR international conference on DNS/LES.
- Spalart P. R., Deck S., Shur M. L., Squires K. D., Strelets M. K., and Travin A. (2006). A new version of detached-eddy simulation, resistant to ambiguous grid densities. *Theoretical and Computational Fluid Dynamics*. 20 (3): 181–195. <https://doi.org/10.1007/s00162-006-0015-0>.
- Taira K., Brunton S. L., Dawson S. T. M., Rowley C. W., Colonius T., et al. (2017). Modal analysis of fluid flows: an overview. *AIAA Journal*. 55 (12): 4013–4041. <https://doi.org/10.2514/1.J056060>.
- Tan C. S., Day I., Morris S., and Wadia A. (2010). Spike-type compressor stall inception, detection, and control. *Annual Review of Fluid Mechanics*. 42 (1): 275–300. <https://doi.org/10.1146>.
- Tang Y. and Liu Y. (2022). VR helicity density and its application in turbomachinery tip leakage flows. *Chinese Journal of Aeronautics*. 35 (11): 1–17. <https://doi.org/10.1016/j.cja.2022.05.006>.
- Tong Z., Lin F., Chen J., and Nie C. (2007) The self-induced unsteadiness of tip leakage vortex and its effect on compressor stall inception. In ASME Paper No. GT2007-27010. <https://doi.org/10.1115/gt2007-27010>.
- Wang G. and Liu Y. (2022). A grid-adaptive simulation model for turbulent flow predictions. *Physics of Fluids*. 34 (7): 075125. <https://doi.org/10.1063/5.0090485>.
- Wang B., Wu Y., Yang F., and Spence S. (2021). Intermittent breakdown of the tip leakage vortex and the resultant flow unsteadiness in the tip-region of a subsonic compressor cascade. *Aerospace Science and Technology*. 113: 106679. <https://doi.org/10.1016/j.ast.2021.106679>.
- Wisler D. C. (1985). Loss reduction in axial-flow compressors through low-speed model testing. *Journal of Engineering for Gas Turbines and Power*. 107 (2): 354–363. <https://doi.org/10.1115/1.3239730>.
- Xie N., Tang Y. and Liu Y. (2023). High-fidelity numerical simulation of unsteady cavitating flow around a hydrofoil. *Journal of Hydrodynamics*. 35 (1): 1–16. <https://doi.org/10.1007/s42241-023-0014-2>.
- Zhang H., Deng X., Lin F., Chen J., and Huang W. (2006). A study on the mechanism of tip leakage flow unsteadiness in an isolated compressor rotor. In ASME Paper No. GT2006-91123. <https://doi.org/10.1109/icccn.2006.286315>.
- Zhang S., Chen H., Ma Z., Wang D., and Ding K. (2022). Unsteady flow and pressure pulsation characteristics in centrifugal pump based on dynamic mode decomposition method. *Physics of Fluids*. 34 (11): 112014. <https://doi.org/10.1115/1.4037973>.
- Zhong W., Liu Y., and Tang Y. (2024). Unsteady flow structure of corner separation in a highly loaded compressor cascade. *Journal of Turbomachinery*. 146 (3): 031003. <https://doi.org/10.1115/1.4063926>.